Engineering Structures 339 (2025) 120638

Contents lists available at ScienceDirect

Engineering Structures

journal homepage: www.elsevier.com/locate/engstruct

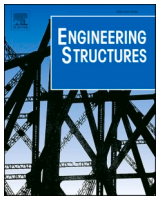

Predictive equations for rotation and sliding of shallow footings under seismic loads using Bayesian regression and ANN

Hamid M. Madani [a], Lydell Wiebe [a,*], Peijun Guo [a], Sanda Koboevic [b]

[a] Department of Civil Engineering, McMaster University, Hamilton, ON, Canada
[b] Department of Civil Engineering, Polytechnique Montreal, Montreal, QC, Canada

ARTICLE INFO

Keywords:
Soil-structure interaction (SSI)
Concentrically braced frames (CBFs)
Bayesian regression
Artificial neural network (ANN)
Footing movement

ABSTRACT

Accurate estimation of footing movement is essential for evaluating its contribution to story drift, which is a critical metric for seismic design. For this reason, this study develops predictive equations to estimate the rotation and sliding of shallow foundations under the combination of seismic and gravity loads. Archetype low-rise concentrically braced frame buildings with shallow footings are designed for Vancouver, Canada, and are modeled using OpenSees. Uncertainty in demand and capacity of the buildings is considered using incremental Latin hypercube sampling (iLHS). A range of footing sizes, from small foundations designed per the US code to larger capacity-protected (CP) footings following the Canadian code, are analyzed to ensure comprehensive coverage of footing size for deriving reliable equations. Two soil sites are considered to account for varying soil conditions. Bayesian regression is used to develop reliable equations for footing rotation and sliding. An artificial neural network (ANN) model further improves prediction accuracy by incorporating complex variable combinations beyond Bayesian regression. Both new approaches are compared to the guidance in the commentary of CSA A23.3, as there is little guidance in the US and other international standards. This study concludes that both current guidance and the proposed new equations accurately estimate footing rotation for CP footings when sliding is minimal. However, the existing guidance tends to underestimate the rotation of smaller footings and does not adequately estimate the footing movement when significant sliding occurs. Therefore, the equations developed here are recommended for a more accurate estimate of footing movement under seismic load.

1. Introduction

The performance of buildings during earthquakes is of utmost importance for fostering resilient cities. The performance-based earthquake engineering (PBEE) methodology, as outlined by Miranda and Aslani [1], provides a probabilistic assessment framework that enables the design of structures with predictable performance levels. Decision-makers and stakeholders commonly rely on quantitative metrics such as repair cost and recovery time to evaluate the performance of structures [2–4]. These metrics are directly influenced by the extent of damage to the building components. The structural response can be characterized by engineering demand parameters (EDPs), such as drift and acceleration, which are used to estimate the level of damage to both structural and non-structural components [5]. These EDPs are affected by the selection of members (e.g., the footing size) for both the superstructure and the substructure of the building [5,6].

The footing size is one of the factors affecting the EDPs and, consequently, the overall performance of a building during seismic events [6–10]. The design load of footings varies significantly depending on building codes and regulations. For example, in the US, footings are typically designed to withstand a reduced seismic design load, allowing the substructure to play a major role in energy dissipation. Conversely, the Canadian code distinguishes between two types of footings: capacity-protected (CP) and not capacity-protected (NCP), both aiming to ensure that the superstructure is the main contributor to energy dissipation [8]. Regardless of the design philosophy, one critical factor in foundation design is the movement of footings under seismic excitation, as it directly impacts the stability of the structure.

A few studies [11–14] have analytically investigated the footing rotation under seismic load. Studies by Allotey and El Naggar [11], Pender et al. [12], and Bazargani [13] propose methods for estimating the rotation of foundations; however, these methods are complex and do not account for the sliding movement of the footings. Adebar [14] proposed simplified methods to calculate the rotation of foundations for

* Corresponding author.
E-mail addresses: moafimas@mcmaster.ca (H.M. Madani), wiebel@mcmaster.ca (L. Wiebe).

https://doi.org/10.1016/j.engstruct.2025.120638
Received 19 December 2024; Received in revised form 21 April 2025; Accepted 21 May 2025
Available online 30 May 2025

reinforced concrete shear walls, and these equations have been incorporated into the Canadian concrete design standard (CSA A23.3:19 [15]) and its commentary [16]. Engineers commonly apply these equations to estimate footing rotations across various structural systems. However, these equations were developed for Canadian CP footings and have not been validated for other types of footings. For Canadian NCP footings, the footing rotation is taken as the largest of the following values: the rotation estimated from these equations, 50% of the displacement at the top of the seismic force-resisting system (SFRS) for a fixed-base model divided by the height above the footing, and 0.005 rad. Although the footing sliding can also contribute significantly to overall seismic drift [6–10], predictive equations are not available for estimating this sliding displacement during design.

Despite the critical role of foundation movement in structural response and building resilience and the wide range of accepted foundation design approaches, methods to accurately estimate footing movements remain limited. To address this gap, this study proposes predictive equations for estimating both the rotation and sliding of footings. Short-period concentrically braced frame (CBF) buildings in Vancouver, BC, are designed per the Canadian National Building Code (NBC 2020 [17]) and steel design standard (CSA S16:19 [18]). Two sites, one near the class C/D boundary (stiff soil) and the other near the class D/E boundary (soft soil), are selected to investigate the effects of soil conditions. Nonlinear response history analysis is used to compute the seismic response, using incremental record-wise Latin Hypercube Sampling (iLHS) with a set of 60 ground motions to address the uncertainty in both the system's demand and capacity. Empirical equations to predict the footing movement are developed using both Bayesian regression and artificial neural network (ANN) techniques. These equations are then compared to the existing equation in the commentary of CSA A23.3 [16] in terms of accuracy and practicality.

2. Archetype buildings

2.1. Superstructure design

In this study, one-, two-, and three-story CBF archetype low-rise commercial buildings of normal importance ($I_E = 1.0$) were designed for Vancouver, Canada (seismic category SC4) following the provisions of the National Building Code of Canada (NBC 2020 [17]) and Canadian steel standard (CSA S16:19 [18]). Seismic resistance in the east-west direction is provided by moderately ductile, tension-compression X-braced frames, with a ductility (R_d) and overstrength (R_o) factor of 3.0 and 1.3, respectively. These archetypes were located on Site Class D soil (V_{s30} = 180–360 m/s). All the buildings under study had a fundamental period on the plateau of the design spectrum, resulting in an identical seismic coefficient. The equivalent lateral force (ELF) procedure of NBC 2020 was used to determine the seismic base shears. Fig. 1 shows the typical plan view common to all archetypes, along with an elevation view of the 2-story building and the deterministic loads used in the design of the CBFs and gravity framing.

The braced frames were designed following the capacity design approach, allowing the braces to yield, while the other components, such as gusset plates, beams, and columns, were designed to withstand the expected capacity of the braces. The braces were chosen from square hollow structural sections and sized to achieve a demand-to-capacity ratio close to one while minimizing the gross area for a cost-effective design. Beams and columns were selected from wide-flange sections. Table 1 summarizes the final brace, beam, and column selection for studied braced frames.

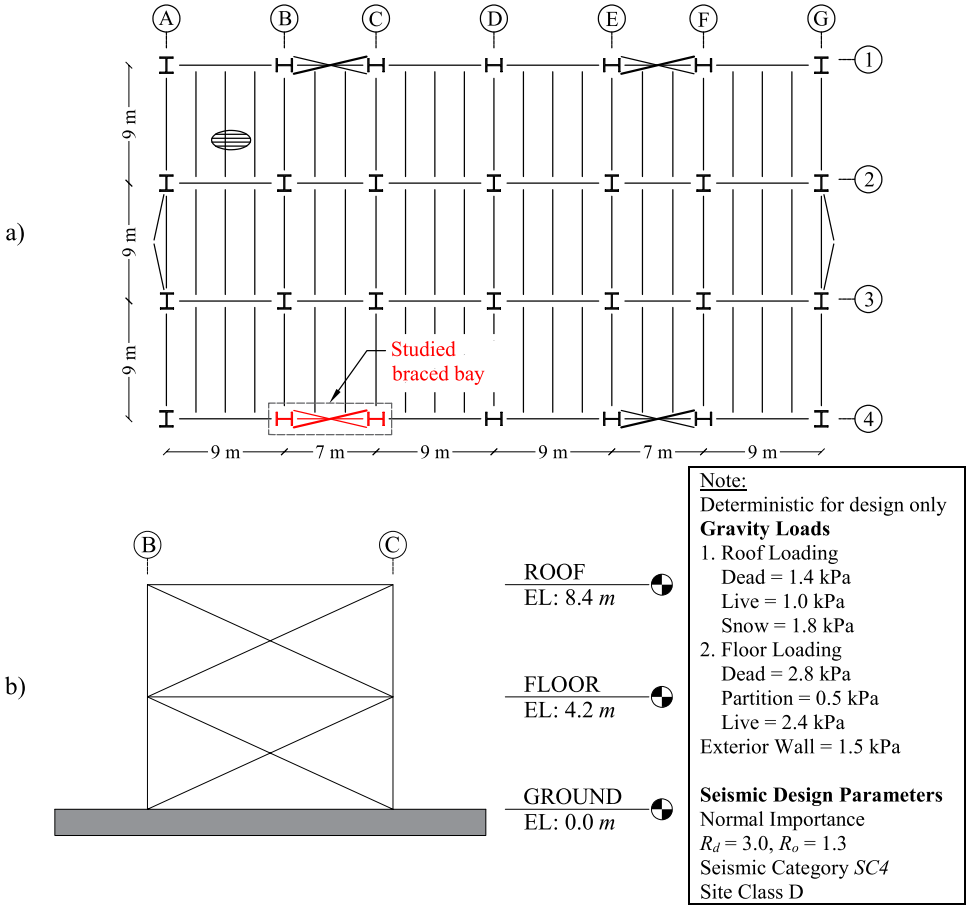

Fig. 1. (a) Typical plan view of all buildings; (b) elevation view of the 2-story buildings.

Table 1
Size of the components selected for the braced frame of the buildings.

Building	Story	Braces	Beams	Columns
3-story	3	HSS 102x102x4.8	W 410 × 39	W 310 × 67
	2	HSS 102x102x9.5	W 410 × 67	W 310 × 143
	1	HSS 127x127x7.9	W 410 × 67	W 310 × 143
2-story	2	HSS 89x89x4.8	W 410 × 39	W 310 × 79
	1	HSS 102x102x7.9	W 410 × 60	W 310 × 79
1-story	1	HSS 76x76x6.4	W 410 × 39	W 250 × 45

2.2. Foundation design

To investigate the impact of soil conditions on the response of the archetypes, two soil types were chosen to represent "stiff" and "soft" sites. Unsaturated clay was selected to represent the soft soil, corresponding to the site class D/E boundary, with average shear wave velocity (V_{s30}) = 200 m/s, undrained shear strength (c) = 35 kPa, unit weight (γ) = 16 kN/m^3, and Poisson's ratio (ν) = 0.4, while dense sand with V_{s30} = 340 m/s, friction angle (ϕ) = 35 deg, unit weight (γ) = 18 kN/m^3, and Poisson's ratio (ν) = 0.35 represented stiff soil corresponding to the site class C/D boundary. These deterministic values were used for design purposes; however, each parameter was treated as a random variable in the modeling, as discussed later. Footing size was taken as a decision variable with a direct correlation among the dimensions of the footing. The footing size ranged from those designed per the US code, labeled as "US footing" in this study, to those designed according to the Canadian code for the expected capacity of the SFRS, referred to as Canadian capacity-protected (CAN-CP) footings. Additionally, Canadian not capacity-protected (CAN-NCP) footings were designed to validate the assumption of a direct correlation among footing dimensions.

The US footings were designed according to ASCE 7–22 [19], using the seismic design load from the ELF procedure, a common practice that does not account for brace expected capacity or overstrength. As permitted by ASCE 7, a 25% reduction was applied to the moment demand on the footing due to the use of the ELF procedure. In contrast, the CAN-NCP and CAN-CP footings were designed in accordance with NBC 2020 and the concrete design standard (CSA A23.3 [15]). CAN-CP footings were sized to resist the probable capacity of the braces in addition to the factored gravity loads from the earthquake load combination. CAN-NCP footings, on the other hand, were designed to withstand factored gravity loads and the larger of either 75% of each braced frame's nominal moment capacity or the overturning moment corresponding to R_dR_o = 2.0. The footing sizes for all the buildings in this study are listed in Table 2.

2.3. Nonlinear building model

A 2D analytical model was developed in OpenSees [20] to investigate the archetype buildings. The seismic mass was determined based on 1.0D + 0.25S, where D represents the dead load and S is the snow load, in line with NBC 2020 guidelines. In this study, gravity loads (dead and live loads) and structural properties, including steel modulus of elasticity and yield strength, were treated as random variables. Table 3 lists the probability distribution functions and their parameters for the selected superstructure variables. The model incorporated gravity framing and P-Delta effects as per the approach proposed by Elkady and Lignos [21], assuming interior gravity columns bend about their weak axis. Rayleigh damping, proportional to the tangent stiffness and mass matrices, was applied to reflect the inherent damping of the building [22], using a triangular distribution of damping ratio with lower, peak, and upper limits of 0.5%, 2%, and 3.5%, respectively.

Table 2
Dimensions of the footings for all buildings (L = length, B = width, H = depth).

		Footing sizes (m) (L*B*H)		
		US	CAN-NCP	CAN-CP
3-story	stiff	13.7 * 3.4 * 0.8	16.5 * 5.4 * 0.9	17.5 * 5.5 * 1.0
	soft	15.6 * 4.6 * 0.8	17.9 * 5.2 * 0.9	18.2 * 5.7 * 1.0
2-story	stiff	12.0 * 1.9 * 0.6	13.8 * 3.8 * 0.9	14.7 * 4.5 * 1.0
	soft	13.4 * 2.7 * 0.6	14.7 * 3.4 * 0.8	15.5 * 3.7 * 0.9
1-story	stiff	11.0 * 1.0 * 0.4	12.5 * 1.6 * 0.8	13.8 * 2.2 * 1.0
	soft	11.0 * 1.0 * 0.4	12.5 * 1.2 * 0.6	13.8 * 1.6 * 0.8

Fig. 2 summarizes the key numerical model assumptions, including gravity framing, soil, and foundation. The braces were modeled with a distributed plasticity model as proposed by Sen et al. [23], using 16 displacement-based beam-column elements, each with four integration points and 128 fibers at each cross-section. The *Steel02* material with 1 % kinematic strain hardening was assigned to these fibers, and an initial out-of-straightness of 0.002 L, where L is the effective length of the brace. Brace fracture was captured by tracking the maximum strain range of the fibers, as suggested by Sen et al. [23]. Gusset plate connections were modeled based on Hsiao et al. [24], with nonlinear rotational springs using *Steel02* material at each brace end, and connection stiffness and strength determined from the connection geometry and material properties.

The beams were modeled with a distributed plasticity approach, using five displacement-based beam-column elements, each with five integration points and *Steel02* material assigned to the fibers. Columns were represented following Lignos and Krawinkler [25] with an elastic beam-column element connected to a zero-length rotational spring at each end. The end springs used the modified Ibarra-Medina-Krawinkler (IMK) material model, with parameters calculated as per NIST GCR 17–917–46v2 guidelines [26] and Lignos et al. [27]. Shear-tab connections in the gravity framing were modeled following Liu and Astaneh-Asl [28], using parameters obtained from Elkady and Lignos [21].

The soil and foundation were modeled using the Beam on Nonlinear Winkler Foundation (BNWF) method, as described by Harden et al. [29] and Gajan et al. [30], capturing vertical settlement, soil energy dissipation, footing flexibility, as well as foundation rotation and sliding. The reinforced concrete foundation is modelled using linear elements, an assumption that is justified in this study because the maximum soil resistance beneath the footing does not exceed the ultimate bearing capacity for which the footings are designed. The fact that NCP and CP footings in Canadian design are heavily reinforced, with applied demands remaining below their factored resistance, also supports the simplification of linear elements. Additionally, for lightly reinforced US footings, the study by Wichman et al. [31] suggests that footing damage did not limit the rocking system's ductility, even when the soil resistance exceeded the ultimate bearing capacity. These factors suggest that the assumption of linearity in the reinforced concrete foundations is unlikely to significantly affect their computed response.

The soil underneath the footing is modeled using vertical zero-length nonlinear springs, with *QzSimple2* material [32] to capture the settlement and rocking of the footing, while two horizontal nonlinear springs represent soil sliding resistance. The frictional sliding resistance beneath the footing and passive soil resistance along its sides were modeled using the *TxSimple1* and *PxSimple1* materials, respectively. The soil properties were treated as random variables in the analysis. The lognormal distribution parameters of the soil properties for both types of soils, alongside the concrete compressive strength of the footing, are listed in Table 4. The mechanical soil properties, including stiffness and strength, were calculated using established geotechnical equations [33–35]. In this study, the small-strain shear modulus was adjusted to account for the reduction caused by large soil shear strains during seismic events. Additionally, radiation damping ratios of 4 % for stiff and 9 % for soft sites were assumed. A detailed description of how the soil mechanical properties and the nonlinear characteristics of the soil material were defined can be found in the thesis by Madani [36].

Table 3
Parameters for the probability distribution function of the selected superstructure random variables.

#	Superstructure Parameter	Notation	Distribution	Mean	COV[a]	LL[b]	UL[c]
1	Modulus of elasticity of steel	E (GPa)	Normal	200	0.05	0	–
2	Floor dead load	DL_F (kPa)	Normal	3.8	0.10	0	–
3	Exterior wall dead load	DL_EW (kPa)	Normal	1.5	0.10	0	–
4	Floor live load	LL_F (kPa)	Gamma	2.4	0.25	–	–
5	Snow load	SL (kPa)	Lognormal	1.8	0.73	–	–
6	Brace expected yield strength	Fy_Br (MPa)	Normal	460	0.10	350	620
7	Gusset plate expected yield strength	Fy_GP (MPa)	Normal	385	0.10	300	440
8	Damping ratio	ξ (%)	Triangular	2.0	–	0.5	3.5

[a] Coefficient of variation
[b] Lower limit
[c] Upper limit

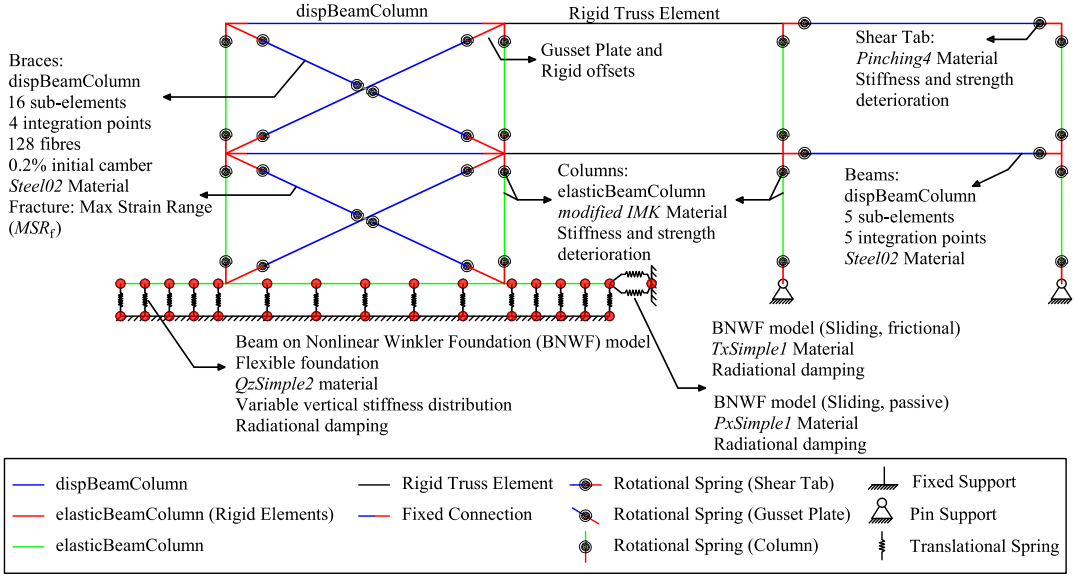

Fig. 2. Analytical model of the archetype buildings.

Table 4
Parameters for the probability distribution function of the selected substructure random variables.

#	Soil Parameter	Notation	Stiff				Soft			
			Median	COV	LL	UL	Median	COV	LL	UL
1	Friction angle	ϕ (deg)	35	0.10	30	42	5	0.20	0	10
2	Cohesion	c (kPa)	5	0.30	0	10	35	0.30	10	50
3	Initial shear modulus	G_0 (MPa)	212	0.25	134	238	65	0.25	53	119
4	Poisson's ratio	ν	0.35	0.30	0.3	0.4	0.4	0.30	0.35	0.45
5	Unit weight	γ (kN/m^3)	18	0.06	16	22	16	0.06	12	18
6	Concrete compressive strength	f'_c (MPa)	32.5	0.15	20	50	32.5	0.15	20	50

2.4. Ground motion selection and scaling

A set of 60 ground motions was selected and scaled for the nonlinear response history analysis. The archetype buildings, located in Vancouver, Canada, experience seismic hazards from crustal, subduction in-slab, and subduction interface earthquakes [37]. Therefore, the selected ground motions primarily included crustal and in-slab ground motion records, with a smaller subset of interface events, reflecting the seismic hazard profile of low-rise structures. Ground motions were drawn from the NGA-West2 [38], K-NET, KiK-net [39], and CESMD [40] databases. Selection and scaling followed the methodology by Baker and Lee [41], with scaling factors ranging from 0.5 to 4.0. Fig. 3 compares the scaled ground motion records to the target spectrum. The records undershoot the target spectrum only at periods far beyond the fundamental period of the buildings investigated in this study, which ranged from 0.20 s to 0.42 s.

2.5. Incremental record-wise Latin hypercube sampling (iLHS)

Incremental record-wise Latin hypercube sampling (iLHS) proposed by Vamvatsikos [42] was used to account for variable uncertainty. Unlike conventional Monte Carlo simulations, which analyze each model sample with a full record suite at a fixed intensity, iLHS applies Latin hypercube sampling simultaneously to both structural properties and seismic inputs, offering greater computational efficiency. Furthermore, iLHS simplifies optimal sample size determination by avoiding the iterative or excessive sampling often required in traditional LHS [42]. The scaled ground motion records were treated as random variables with a uniform distribution. The gravity load on the building and the material properties of the superstructure and substructure were also

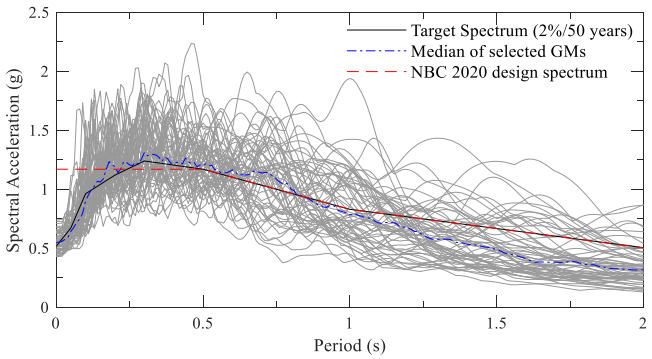

Fig. 3. Selected ground motions scaled to match the target spectrum.

taken into account as random variables, as discussed earlier.

The iLHS method begins with a small sample size, doubling with each generation until the desired accuracy is attained. Here, the iLHS was conducted following the method proposed by Kazantzi et al. [43], starting with 10 samples and subsequently doubling the size by adding 10, 20, and so forth. In this study, the number of samples depends on the change in the median of drift and acceleration from one generation to the next. If the change in the output of interest is less than the desired tolerance, then the process comes to an end. This iterative process required six generations totaling 320 samples, significantly fewer than with conventional LHS [44]. Minor changes in the drift and acceleration distribution parameters from the fourth to the fifth generation confirmed that the sample size was adequate to achieve a reliable response characterization.

2.6. Bayesian linear regression

The analysis results were used to develop predictive equations for footing movements (response variables) across a wide range of footing sizes. Bayesian linear regression was initially employed to derive empirical equations for estimating these response variables. Various linear equations were tested, with the form shown in Eq. (1) emerging as the most suitable. To apply the Bayesian linear regression, however, a linear form was required, leading from Eq. (1) to Eq. (2). In these equations, Y is the model response or output, X_1 to X_N are the explanatory or predictor variables, θ_1 to θ_{N+1} are the model parameters or regression coefficients, and ε is the model error or residual [45]. Bayesian linear regression aims to determine the posterior distribution of these parameters rather than a single best value. A key advantage of Bayesian regression is that with the acquisition of new data, the equation can be updated, allowing continuous refinement of the predictive model [46].

$$Y = \theta_1 (X_1)^{\theta_2} (X_2)^{\theta_3} \ldots (X_N)^{\theta_{N+1}} \tag{1}$$

$$\ln(Y) = \ln(\theta_1) + \theta_2 \ln(X_1) + \theta_3 \ln(X_2) + \ldots + \theta_{N+1} \ln(X_N) + \varepsilon \tag{2}$$

To perform this regression, parameters influencing the model response were selected as potential explanatory variables. Dimensional analysis using the Buckingham Pi Theorem was carried out to convert these parameters into a dimensionless form. A t-distribution was then used to determine the distribution parameters for the regression coefficients, and the coefficient of variation (COV) was calculated for each. The predictor variable corresponding to the model parameter with the highest COV was iteratively removed until a significant change appeared in the mean or standard deviation of the model error or until the model accuracy was compromised [47]. To select the best predictive equations, the coefficient of determination (R^2) was evaluated along with tests for normality and heteroskedasticity of residuals, verifying the basic assumptions of the regression method.

2.7. Artificial neural network (ANN)

To capture hidden factors affecting the footing movement and achieve more accurate estimates, an artificial neural network (ANN) was developed as the second method in this study. ANN can identify all possible interactions among predictor variables and detect complex nonlinear relationships between inputs and outputs [48]. First, predictor variables were standardized. Then, a randomly selected 70% of the data (training dataset) was used to train the model, while the remaining 30% of the data (validation dataset) was reserved for validation.

Only one hidden layer was included in this method. The number of neurons was determined by plotting the root mean squared error (RMSE) of both the training and validation datasets. As the number of neurons increases, the RMSE of the training dataset generally decreases. However, the RMSE of the validation dataset initially decreases, indicating that the number of neurons is insufficient to fit the data (underfitting); then, at a certain point, the RMSE starts to increase (overfitting). The number of neurons corresponding to the lowest RMSE for the validation dataset was selected for the hidden layer. The ANN models for predicting the footing sliding and rotation can be accessed at the following GitHub repository: https://github.com/Hamid-M-Madani/ANN-rotation-sliding.

2.8. Predictor variables definition and selection

As shown in Fig. 4a), the footing rotation can be calculated from the maximum settlement (Δ_{max}) and contact length (c) using Eq. (3). Following Bazargani [13], a new parameter (γ) is defined, which is $\Delta_{\max}$ normalized by the displacement z_{50} when 50 % of the soil's ultimate bearing capacity is mobilized. The parameter z_{50} can be estimated using Eq. (4), as suggested by Gajan et al. [30], where $q_{ult,s}$ and k_s are the ultimate bearing capacity and vertical stiffness of the soil springs, respectively. By determining the equivalent uniform stress distribution (Fig. 4b) and substituting the parameters from Eq. (4) into Eq. (3), the footing rotation can then be calculated using Eq. (5). In this study, the new parameter $\psi_{rotation}$ (Eq. (6)) was defined to help estimate the maximum rotation of the footing. As an analogy to $\psi_{rotation}$, a normalized sliding parameter, $\psi_{rotation}$, was also defined in Eq. (7), with $\Delta_{\max}^{sliding}$ and $z_{50}^{sliding}$ being the maximum horizontal displacement and z_{50} of the frictional sliding spring, respectively.

$$\theta = \frac{\Delta_{\max}}{c} \tag{3}$$

$$\gamma = \frac{\Delta_{\max}}{z_{50}}, \quad z_{50,clay} = 0.525 \frac{q_{ult,s}}{k_s}, \quad z_{50,sand} = 1.39 \frac{q_{ult,s}}{k_s} \tag{4}$$

$$\theta = \frac{\Delta_{\max}}{c} = \frac{\gamma z_{50}}{a/\beta} = \beta\gamma \frac{z_{50}}{a}, \text{ where } a = L - \frac{2M}{P} \tag{5}$$

$$\psi_{rotation} = \beta\gamma \tag{6}$$

$$\psi_{sliding} = \Delta_{\max}^{sliding} \Big/ z_{50}^{sliding} \tag{7}$$

As discussed, dimensional analysis was conducted to identify

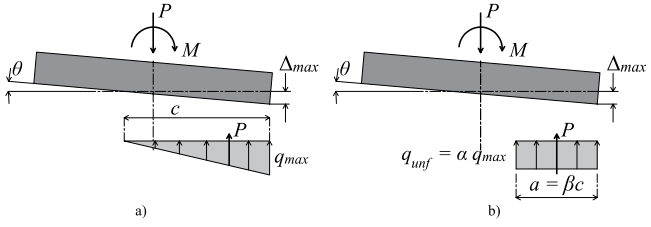

Fig. 4. a) Triangular stress distribution b) equivalent uniform stress distribution of soil.

potential explanatory variables for the equations. Then, the dependency of the model response, i.e., $\psi_{sliding}$ and $\psi_{rotation}$, on these potential explanatory variables was investigated. These variables include, but are not limited to, those listed in Table 5. The permutation of the parameters shown in this table was also used to construct and investigate new variables. In this table, L_f, B_f, and H_f represent the footing's length, width, and depth, respectively, while a represents the length of the equivalent uniform bearing stress block. Moreover, q_{ult} is the soil's overall ultimate bearing capacity, which is different from the ultimate bearing capacity of the springs ($q_{ult,s}$) defined earlier. The remaining parameters were defined in Table 4. Even variables with minimal impact on the model response were initially selected for the Bayesian regression process, though low-impact parameters were later removed as described previously. Fig. 5 illustrates the dependency of the model response on parameters ultimately included in the final equations for rotation and sliding using Bayesian regression.

Fig. 5a) indicates a strong negative correlation between the logarithmic form of $q_{ult}/0.001G_0$ and $\psi_{rotation}$. Here, q_{ult} is the overall ultimate bearing capacity of the soil, and G_0 is the soil's initial shear modulus. The quotient $q_{ult}/0.001G_0$ reflects the effects of soil bearing capacity and stiffness on footing rotation. Fig. 5b) and Fig. 5d) show that q_{unf}/q_{ult} and 1-T_f/T_{ult} are key variables for estimating $\psi_{rotation}$ and $\psi_{sliding}$, respectively. In these expressions, q_{unf} represents the magnitude of the equivalent uniform stress, T_f denotes the maximum frictional sliding force, and T_{ult} is the ultimate frictional sliding resistance force. Bayesian regression indicates that 1-T_f/T_{ult} provides a more accurate estimate for sliding than T_f/T_{ult}. Fig. 5c) shows a significant negative correlation between $T_{ult}/0.001G_0L_fB_f$ and $\psi_{sliding}$. The parameter $T_{ult}/0.001G_0L_fB_f$ represents the effects of soil strength and stiffness on the footing sliding. Since T_{ult} has units of force and G_0 has units of pressure, the parameters L_f and B_f were used to render this parameter dimensionless.

3. Predictive equations for rotation and sliding

3.1. Rotation of the footing: Bayesian regression

The Bayesian linear analysis reveals that $\psi_{rotation}$ can be estimated by Eq. (8), with the posterior mean and COV of σ (the regression coefficient of ε) of 0.37 and 1.67 %, respectively.

$$\psi_{rotation} = \exp(\theta_5)\left(\frac{q_{ult}}{0.001\cdot G_0}\right)^{\theta_1}\left(\frac{L_f}{B_f}\right)^{\theta_2}\left(\frac{a}{B_f}\right)^{\theta_3}\left(\frac{q_{unf}}{q_{ult}}\right)^{\theta_4} \tag{8}$$

To avoid overfitting the data and validate Eq. (8), 15% of the data points were randomly excluded from the dataset and designated as examiners to assess the accuracy of the predictive equation. Various equation formulations were tested, but as previously discussed, the form in Eq. (1) proved most suitable. Assuming a t-distribution posterior, the mean and COV of the regression coefficients, along with their correlations, are presented in Table 6.

To simplify the equation given in Eq. (8), terms were removed until the COV of the model parameter (θ_i) with the highest COV (=14 %) was less than the mean of σ (=0.37), as further reduction could compromise the model's quality [47]. The final predictor variables have physical meaning: q_{ult}/G_0 incorporates soil properties, L_f/B_f reflects the impact of the footing's aspect ratio on rotation, and a/B_f and q_{unf}/q_{ult} capture the effects of the force demand on the footing rotation, tracked through the length and magnitude of the uniform bearing stress distribution. The negative value of θ_1 indicates that higher magnitudes of q_{ult}/G_0 decrease $\psi_{rotation}$, whereas the positive estimate of θ_4 suggests that increasing q_{unf}/q_{ult} increases the output; both observations are in agreement with the trends seen in Fig. 5. Analysis of Eq. (8) shows a strong correlation between θ_1 and θ_4 (ρ = 0.867), which is expected given the definitions of these parameters. According to Gardoni et al. [47], when two parameters are strongly correlated, one can be replaced with the other. However, this replacement was not applied in this study, as it is primarily useful for the probabilistic forms of the equation, not for the deterministic forms used by practicing engineers.

Table 5
Selected potential explanatory variables for $\psi_{rotation}$.

	Potential Variable		Potential Variable		Potential Variable
1	ν	5	a/B_f	9	c/q_{ult}
2	G_0/q_{ult}	6	q_{unf}/q_{ult}	10	$M/\left(q_{ult}B_f^3\right)$
3	L_f/B_f	7	$\gamma B_f/q_{ult}$	11	$P/\left(q_{ult}B_f^2\right)$
4	H_f/B_f	8	ϕ	12	f_c'/q_{ult}

Fig. 6a) compares the observed and predicted values of $\psi_{rotation}$. Data points lying close to the line of unity and a high coefficient of determination ($R^2 = 0.94$) indicate a reliable and accurate prediction. In this figure, blue dots represent the training dataset, while the red stars represent the validation dataset, allowing potential outliers to be identified. The model shows greater error for small values of rotation (i.e., $\psi_{rotation}$), suggesting slightly reduced accuracy for very small footing rotations, where precision is less critical.

The predictive equation's compliance with the linear regression assumptions was also confirmed (Fig. 6b and Fig. 6c). Fig. 6b) illustrates the quantile-quantile plot, showing the normality of the model error. Most data points align closely with the line of unity, although slight deviations from normality occur at smaller values of $\psi_{rotation}$. Homoskedasticity of the residuals across all predictor variables was also verified, as shown in Fig. 6c), where residuals form a horizontal band, indicating consistent variance across predictor values.

A sensitivity analysis was performed using the algorithm proposed by Schmidt and Lipson [49] to identify the most influential parameters. The results for the model in Eq. (8) are shown in Table 7. In this table, the "Positive" column indicates the likelihood that increasing a variable raises the output, while the "Negative" column reflects the likelihood of a decrease. The analysis shows that increasing q_{ult}/G_0 and a/B_f always reduces $\psi_{rotation}$, whereas increasing L_f/B_f and q_{unf}/q_{ult} has the opposite effect. Notably, q_{unf}/q_{ult} is identified as the most impactful parameter for predicting footing rotation, consistent with the trend observed in Fig. 5b), where this parameter alone demonstrates strong predictive power.

3.2. Rotation of the footing: ANN

Fig. 7 illustrates the predicted versus observed values for $\psi_{rotation}$ using the ANN-trained model. The model outperforms the Bayesian regression in terms of R^2 accuracy, as it incorporates physical features derived from combinations of predictor variables not directly considered in Bayesian regression. The optimal number of neurons for predicting $\psi_{rotation}$ was determined to be 18, based on the minimum RMSE. For this model, in addition to the variables from Table 7, the soil's Poisson's ratio (ν) was included to incorporate physically meaningful variables into the ANN fitting process.

3.3. Sliding of the footing: Bayesian regression

Eq. (9) provides an estimate for $\psi_{sliding}$ using the Bayesian linear regression method. The equation yields a posterior mean of 0.49 and a COV of 1.63 % for σ (the regression coefficient of ε). In this equation, T_f denotes the maximum frictional sliding force. Similar to Eq. (8) for the footing rotation, 15 % of the data points were randomly excluded from the dataset to validate and assess the equation's accuracy. It is also identified that the form shown in Eq. (1) yielded the most reliable results. Assuming a t-distribution posterior, Table 8 presents the mean, COV, and correlations of the regression coefficients.

$$\psi_{sliding} = \exp(\theta_3)\left(\frac{T_{ult}}{0.001\cdot G_0\cdot L_f\cdot B_f}\right)^{\theta_1}\left(1-\frac{T_f}{T_{ult}}\right)^{\theta_2} \tag{9}$$

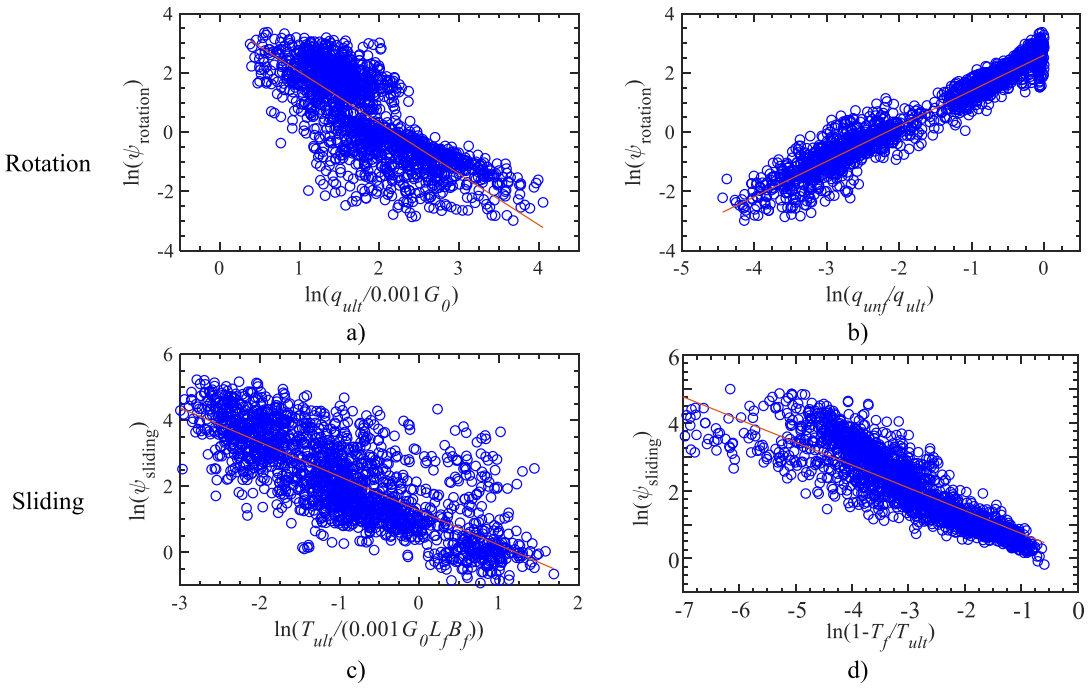

Fig. 5. Dependency of $\psi_{rotation}$ on a) q_{ult}/G_0 and b) q_{unf}/q_{ult}; and $\psi_{sliding}$ on c) T_{ult}/G_0 and d) 1-T_f/T_{ult}.

Table 6
Posterior statistics of parameters in $\psi_{rotation}$ model of Eq. (8).

Parameter	Mean	COV(%)	Correlation				
			θ_1	θ_2	θ_3	θ_4	θ_5
θ_1	−0.30	9.10	1				
θ_2	0.30	10.06	−0.315	1			
θ_3	−0.22	14.21	0.655	−0.699	1		
θ_4	1.02	1.66	0.867	−0.489	0.764	1	
θ_5	2.46	2.11	−0.340	−0.741	0.211	−0.002	1

The equation was simplified by gradually removing unnecessary predictor variables until the coefficient of variation (COV) of the parameter with the highest COV (=12 %) fell below the mean of σ (0.49). Further reduction of variables in Eq. (9) was avoided to maintain model quality. The negative estimate of θ_1 suggests that higher values of T_{ult}/G_0 decrease $\psi_{sliding}$, while the negative estimate of θ_2 indicates that increasing T_f/T_{ult} raises the predicted sliding. These findings align with the trends observed in Fig. 5. Table 8 also shows that the model parameters are not strongly correlated ($\rho < 0.7$), except for the constant of the equation (θ_3) and θ_2.

Fig. 8a) compares the observed and predicted values of $\psi_{sliding}$. Most data points align closely with the line of unity, and an R^2 of 0.87 indicates that Eq. (9) derived for footing sliding is both accurate and reliable. The model's accuracy remains consistent across the whole range of $\psi_{sliding}$ values. The underlying assumptions of the linear regression analysis were also verified. Fig. 8b) shows a quantile-quantile plot, suggesting that the residuals follow a Gaussian distribution. As with $\psi_{rotation}$, a slight deviation from normality occurs at small $\psi_{sliding}$ values, but the majority of data points align closely with the line of unity. Additionally, heteroskedasticity was avoided in the development of the predictive equation. As an example, Fig. 8c) illustrates the homoskedasticity of residuals for one predictor variable, showing that the error remains consistent across the range of 1-T_f/T_{ult}.

Similar to the previous section, a sensitivity analysis was carried out to identify the most impactful parameters for $\psi_{sliding}$. The results for the model in Eq. (9) are given in Table 9. The "Positive" and "Negative" columns, as introduced earlier, indicate that increasing T_{ult}/G_0 consistently reduces $\psi_{sliding}$, while increasing T_f/T_{ult} has the opposite effect. The sensitivity analysis highlights T_f/T_{ult} as the most influential parameter for predicting $\psi_{sliding}$, in line with the trend observed in Fig. 5d), where T_f/T_{ult} alone shows a strong predictive capability. The footing geometry, which influences the sliding behavior, is incorporated into Eq. (9) through the footing dimensions L_f and B_f.

3.4. Sliding of the footing: ANN

Fig. 9 illustrates the predicted versus observed values for the ANN model used to estimate $\psi_{sliding}$. As with the ANN model trained for the estimation of $\psi_{rotation}$, this model demonstrates superior accuracy in terms of R^2, compared to the Bayesian regression equation. This improvement, as previously discussed, is due to the ANN's ability to account for physical features with complex patterns or relationships resulting from combinations of predictor variables. The number of neurons in the hidden layer was again chosen based on the minimum RMSE; 17 neurons were found to be optimal for predicting $\psi_{sliding}$.

3.5. Example application of equations

This section provides examples of estimating footing sliding and rotation using models proposed in this study, along with a comparison to the equation in the commentary of CSA A23.3 [16]. In engineering practice, similar analysis can be integrated into foundation design when soil properties are known and an initial footing size has been selected based on bearing capacity checks. These results can then be used to optimize footing design. The limitations of the equations proposed in this study, along with those in the commentary of A23.3, are summarized in Table 10. The equations proposed in this study were developed to cover a range of footing sizes, from US footings to CAN-CP footings, and also to account for sliding. In contrast, the equation in the A23.3 commentary was developed only for CAN-CP footing sizes, with sliding neglected. In the context of this study, one mode (either sliding or rotation) generally dominates the footing movement, with the other mode having a minimal effect [36]. Consequently, the neglect of coupled sliding-rotation effects is not expected to significantly impact the accuracy of the results. Four examples are examined here to

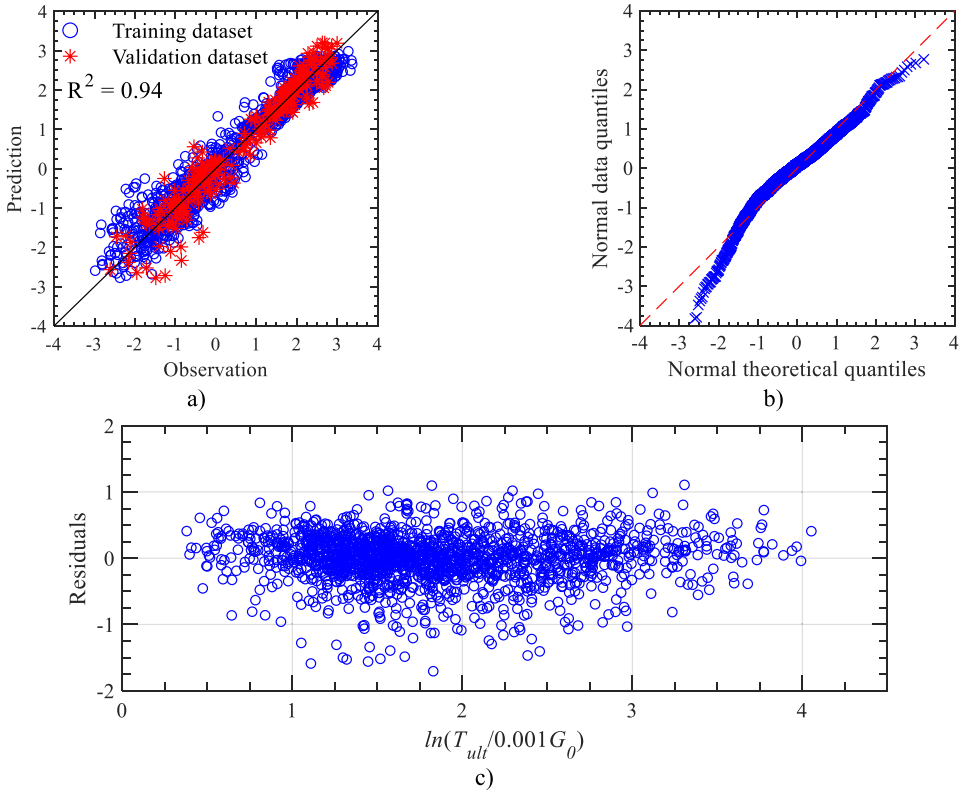

Fig. 6. a) Prediction versus observation of $\psi_{rotation}$ using the Bayesian regression, b) normality test of Eq. (8), and c) the homoskedasticity of residuals for T_{ult}/G_0.

Table 7
Sensitivity analysis of parameters in $\psi_{rotation}$ model of Eq. (8).

Variable	Sensitivity	Positive(%)	Negative(%)
q_{ult}/G_0	0.14	0.0	100
L_f/B_f	0.09	100	0.0
a/B_f	0.08	0.0	100
q_{unf}/q_{ult}	0.85	100	0.0

Table 8
Posterior statistics of parameters in $\psi_{sliding}$ model of Eq. (9).

Parameter	Mean	COV(%)	Correlation		
			θ_1	θ_2	θ_3
θ_1	−0.91	1.24	1		
θ_2	−0.52	1.57	−0.181	1	
θ_3	−0.24	11.56	0.213	0.836	1

illustrate trends in the accuracy of equations across a larger set of cases than are presented. The first example demonstrates that the proposed equations yield estimates closely matching those in the CSA A23.3 commentary when the footing size falls within the range applicable to all methods. The second and third examples assess the proposed equation's performance when footing size is outside the valid range of the equation in the commentary of CSA A23.3. In the first two examples, sliding is minimal, so excluding it does not significantly impact the rotation prediction. In contrast, the third example highlights the limitations of the A23.3 commentary's equation when sliding is the primary contributor to the drift. For the first three examples, the results are compared to those from the numerical analysis described above for a single ground motion. The fourth example checks the validity of the proposed equations against the experimental data. Flowcharts outlining the

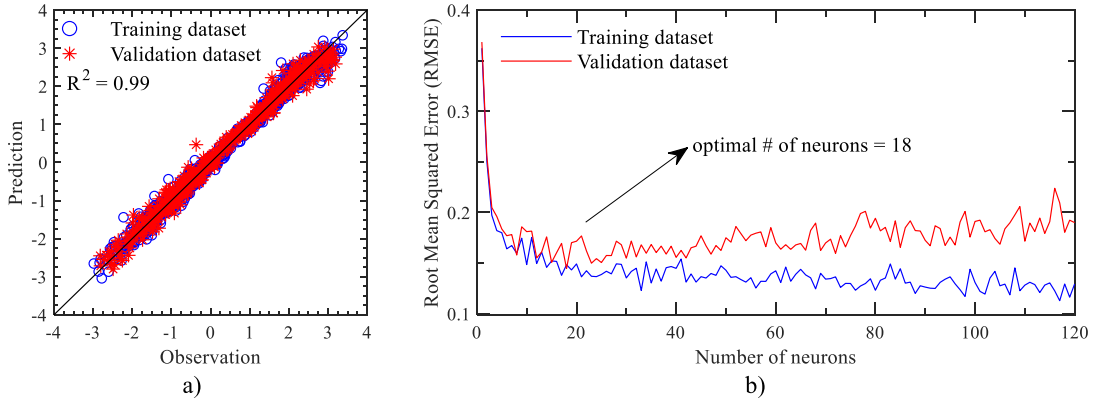

Fig. 7. a) Prediction versus observation of $\psi_{rotation}$ using the ANN, b) the RMSE of training and validation dataset with respect to the number of neurons.

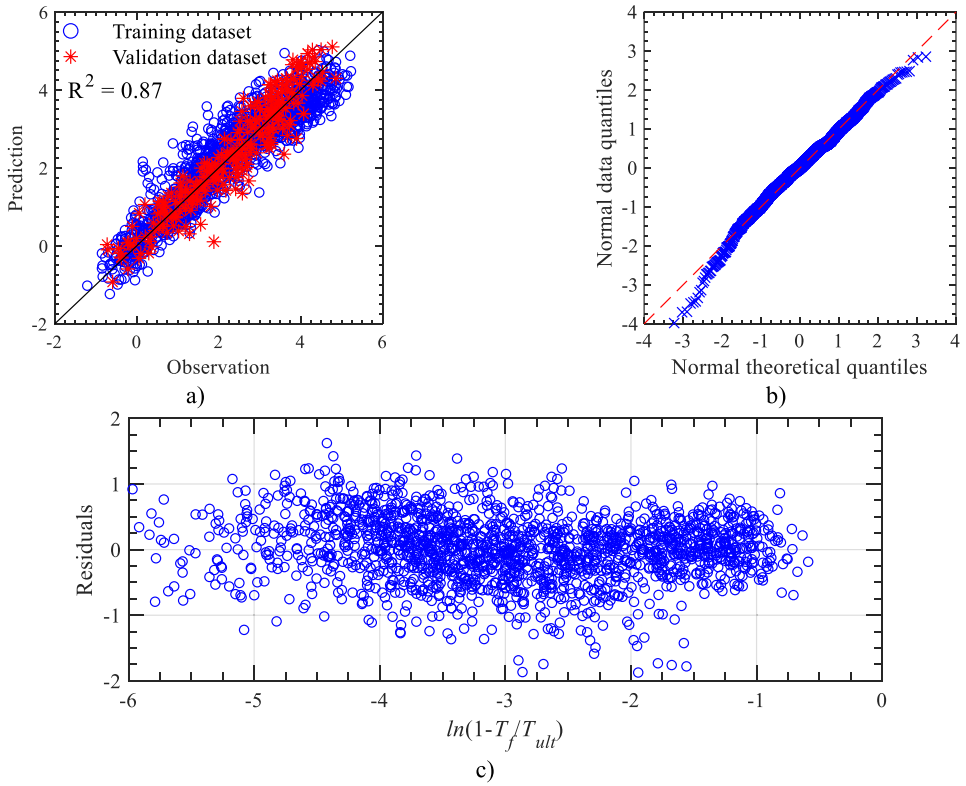

Fig. 8. a) Prediction versus observation of $\psi_{sliding}$ using the Bayesian regression, b) normality test of Eq. (9), and c) the homoskedasticity of residuals for 1-T_f/T_{ult}.

Table 9
Sensitivity analysis of parameters in $\psi_{sliding}$ model of Eq. (9).

Variable	Sensitivity	Positive(%)	Negative(%)
$T_{ult}/(G_0 \cdot L_f \cdot B_f)$	0.57	0.0	100
T_f/T_{ult}	0.72	100	0.0

application of the proposed equations are provided in Appendix A of the thesis by Madani [36].

3.5.1. Example 1: CAN-CP footing on soft soil

The first example examines a CAN-CP footing for a 2-story building on soft soil. A CAN-CP-sized footing (15.5 m long, 3.7 m wide, and 0.9 m deep, as shown in Table 2) was selected to compare the rotation predicted by Eq. (8) and the ANN model with that obtained from the equation in the CSA A23.3 commentary, which was developed specifically for these types of footings. The soil's initial shear modulus and Poisson's ratio are 51 MPa and 0.41, respectively, while the ultimate bearing strength is 180 kPa. The footing is subjected to an overturning moment of 10150 kN.m and a vertical load of 2250 kN. The ultimate frictional sliding resistance is 2240 kN, while the maximum frictional sliding force is 1490 kN.

The stress characteristics at the soil-footing interface and the characteristic settlement z_{50} are determined using Eq. (8). Based on the footing's dimensions and loads, the uniform bearing stress (q_{unf}) and the stress block length (a) are calculated as $q_{unf} = 94$ kPa and $a = 6.5$ m, respectively. Using Eq. (4), the value of z_{50} of the soil beneath the footing is found to be 3.47 mm. With these inputs, Eq. (8) gives $\psi_{rotation} = 4.36$, resulting in a rotation of 0.0023 rad from Eq. (5). Meanwhile, the drift due to sliding for this footing is merely 0.0006 rad. Using the ANN model, the estimated footing rotation and sliding are 0.0020 rad and 0.0008 rad, respectively, closely aligning with the numerical analysis results, which show a rotation of 0.0018 rad and sliding of 0.0010 rad, producing a first-story drift of 0.0028 rad.

The CSA A23.3 commentary recommends the following equation to calculate the rotation of CAN-CP footings:

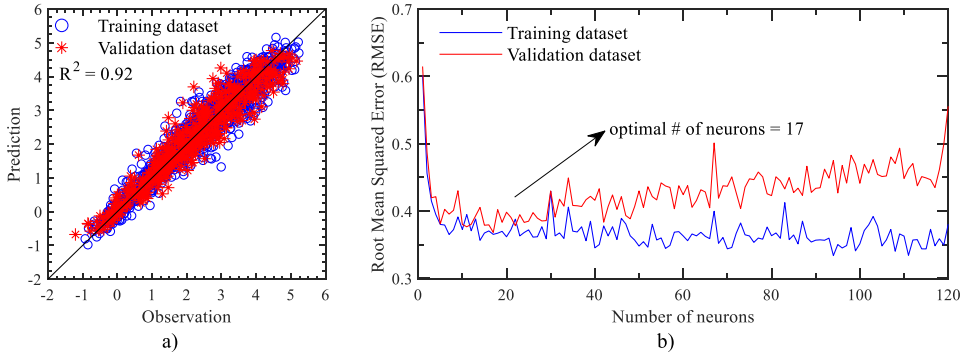

Fig. 9. a) Prediction versus observation of $\psi_{sliding}$ using the ANN, b) the RMSE of training and validation dataset with respect to the number of neurons.

Table 10
Limitations of the methods proposed in this study and the commentary of A23.3 and their difference from the numerical analysis.

			Commentary of CSA A23.3 [16]	Bayesian regression	ANN
Equation(s)			(10)	(8) and (9)	—
Sliding			neglected	considered	considered
Range of valid q_{unf}/q_{ult}			0.25–0.5	0.01–1.0	0.01–1.0
Range of studied q_{unf}/q_{ult}			0.25–1.0	0.01–1.0	0.01–1.0
Range of valid footing size			CAN-CP only	US to CAN-CP	US to CAN-CP
Difference from the numerical analysis	Example 1	Rotation	28 %	28 %	11 %
		Sliding	N/A	−40 %	−20 %
		Total	−18 %	4 %	0 %
	Example 2	Rotation	−49 %	−8 %	−5 %
		Sliding	N/A	−25 %	8 %
		Total	−61 %	−12 %	−2 %
	Example 3	Rotation	−88 %	−13 %	−25 %
		Sliding	N/A	−33 %	−37 %
		Total	−97 %	−29 %	−34 %

$$\theta = 0.2(1-\nu)\left(\frac{q_{unf}}{0.5G_0}\right)\left(\frac{L_f}{a}\right)\xi_L\cdot\xi_{NL} \tag{10}$$

where ξ_{NL} and ξ_L are defined in Eq. (11) and Eq (12).

$$\xi_L = \left(1-1.5\frac{D_f}{L_f}\right)\left(1-0.1\frac{L_f}{B_f}\right) \geq 0.2 \tag{11}$$

$$\xi_{NL} = 1+4\left(\frac{q_{unf}}{q_f}-0.5\right)\left(\frac{a}{B_f}\right)^{1.5} \geq 1.0 \tag{12}$$

According to these equations, ξ_L depends solely on the footing's geometrical characteristics, including its dimensions and buried depth D_f, while ξ_{NL} reflects the stress characteristics at the footing-soil interface, specifically q_{unf} and a normalized by $q_f = 0.5q_{ult}$ and B_f, respectively. Using these parameters, Eq. (10) estimates the rotation as 0.0023 rad, matching the result from Eq. (8). A comparison of footing rotation estimates from the equations proposed in this study and from the CSA A23.3 commentary with the numerical analysis results (Table 10) shows that the values are similar and closely align with the numerical analysis findings. While the CSA commentary does not recommend estimating sliding, the ANN and Bayesian regression underestimate it by 20 % and 40 %, respectively. However, given the small absolute value of sliding relative to the rotation, as well as the small total motion, this discrepancy is not significant overall.

3.5.2. Example 2 CAN-NCP footing on soft soil

The second example examines the movement of a CAN-NCP footing on soft soil, where the equation in the commentary of CSA A23.3 was not derived for such footings. Footing rotation and sliding were estimated using Eqs. (8) and (9), as well as those from the ANN model. This footing is 14.7 m long, 3.4 m wide, and 0.8 m deep (see Table 2). The soil's initial shear modulus and Poisson's ratio are 49 MPa and 0.39, respectively, while the ultimate bearing capacity is set to 356 kPa. The footing is subjected to an overturning moment demand of 9687 kN.m and an axial force of 1955 kN. Additionally, the ultimate frictional sliding resistance is 2969 kN, while the maximum frictional sliding force is 1881 kN.

To calculate the sliding and rotation of the footing, the following parameters are determined: the uniform bearing stress $q_{unf} = 120$ kPa, the uniform bearing stress block length $a = 4.8$ m, z_{50} for the soil beneath the footing as 5.7 mm, and z_{50} of the frictional sliding spring (zt_{50}) as 3.4 mm. Using Eqs. (8) and (9), $\psi_{rotation}$ and $\psi_{sliding}$ are calculated as 3.10 and 1.11, respectively, resulting in a predicted rotation of 0.0036 rad due to footing rotation and 0.0009 rad due to sliding. Meanwhile, the ANN estimates the footing rotation and sliding as 0.0037 rad and 0.0013 rad, respectively. The numerical analysis yields rotation and sliding values of 0.0039 rad and 0.0012 rad, respectively. These values, along with the relative errors shown in Table 10, demonstrate that the proposed equations in this study provide a reasonable estimate of the footing movement. In contrast, the footing movement estimated using Eq. (10) from the CSA A23.3 commentary is 0.0020 rad, significantly lower than the total movement obtained from the numerical analysis. This discrepancy is expected, as Eq. (10) is proposed for CAN-CP footings, which typically exhibit smaller rotations compared to CAN-NCP footings. However, Clause 21.10.3.3.3 of the CSA A23.3 design standard would require 0.005 rad to be considered as a minimum assumed inter-story drift due to rotation of CAN-NCP footings, and this happens to be a good estimate in this case.

3.5.3. Example 3 CAN-NCP footing on stiff soil

The third example investigates the rotation and sliding of a CAN-NCP footing on stiff soil, where sliding contributes significantly to the total drift. Footing rotation and sliding were estimated using Eqs. (8) and (9), as well as those from the ANN model. This rectangular footing is 13.8 m long, 3.8 m wide, and 0.9 m deep (see Table 2). The soil's initial shear modulus and Poisson's ratio are 202 MPa and 0.31, respectively, while the ultimate bearing capacity is set to 1830 kPa. The footing is subjected to an overturning moment demand of 7030 kN.m and an axial force of 2060 kN. Additionally, the ultimate frictional sliding resistance is 1520 kN, while the maximum frictional sliding force is 1088 kN.

To calculate the sliding and rotation of the footing, the following parameters are determined: the uniform bearing stress $q_{unf} = 78$ kPa, the uniform bearing stress block length $a = 7.0$ m, z_{50} for the soil beneath the footing as 15.9 mm, and z_{50} of the frictional sliding spring (zt_{50}) as 0.96 mm. Using Eqs. (8) and (9), $\psi_{rotation}$ and $\psi_{sliding}$ are found to be 0.31 and 8.75, respectively, resulting in a predicted rotation of 0.0007 rad due to footing rotation and a first-story drift of 0.0020 rad due to sliding. Meanwhile, the ANN estimates the footing rotation and sliding as 0.0006 rad and 0.0019 rad, respectively. The numerical analysis yields rotation and sliding values of 0.0008 rad and 0.0030 rad, respectively. These values, along with the relative errors shown in Table 10, demonstrate that the proposed equations in this study provide a reasonable estimate of the footing movement, considering how small the deformations are in this case. In contrast, the footing movement estimated using Eq. (10) from the CSA A23.3 commentary is 0.0001 rad, significantly lower than the total movement obtained from the numerical analysis. This discrepancy suggests that Eq. (10) does not adequately account for footing movement when sliding is significant. Although Clause 21.10.3.3.3 of the CSA A23.3 design standard addresses this limitation with its 0.005 rad inter-story drift requirement for CAN-NCP footings, this value greatly overestimates the actual footing movement in this case. The information regarding the footing sliding is unavailable.

3.5.4. Example 4 Validation with experimental results

The fourth example examines the rotation of a square footing tested by Negro et al. [50] to compare the predictions of the proposed equation with experimental results. This 1 m × 1 m square footing on sand was

subjected to a constant vertical load of 300 kN. According to Adebar [14], the soil had a shear modulus of 90 MPa and a Poisson's ratio of 0.3, while the ultimate bearing capacity was estimated at 1400 kPa. In this example, the footing rotation is validated against experimental results for a case where the footing was subjected to an overturning moment demand of 110 kN·m.

To calculate the footing rotation, the following parameters are determined: the uniform bearing stress $q_{unf} = 1154$ kPa, the uniform bearing stress block length $a = 0.26$ m, and z_{50} for the soil beneath the footing was 0.95 mm. Using Eq. (8), $\psi_{rotation}$ is calculated as 5.67, resulting in a predicted rotation of 0.0208 rad due to footing rotation. Meanwhile, the ANN estimates the footing rotation as 0.0192 rad. The experimental test results indicate a rotation of 0.0200 rad, demonstrating that the proposed equations in this study provide a reasonable estimate of footing rotation.

4. Concluding remarks

This paper proposes predictive equations for estimating the rotation and sliding of shallow footings of short-period concentrically braced steel frames. The archetype buildings were designed deterministically following the National Building Code (NBC 2020), CSA S16:19 (steel superstructure), and CSA A23.3:19 (concrete footings) design standards. Incremental record-wise Latin Hypercube Sampling (iLHS) was employed to address uncertainties in the numerical model, including structural material, gravity loads, seismic loads, and structural damping. Footing sizes ranged from small footings designed per US code to large capacity-protected (CP) footings designed per Canadian code, ensuring comprehensive coverage for developing reliable predictive equations. Two soil conditions were considered: stiff soil near the class C/D boundary and soft soil near the class D/E boundary. Footing rotations and sliding were determined from nonlinear response history analysis conducted in OpenSees. Dimensional analysis identified potential predictive variables, and Bayesian regression was employed to derive equations for estimating the footing movement. Sensitivity analysis was conducted to determine the most influential parameters. An artificial neural network (ANN) was also employed to achieve better predictions of footing movement. The proposed equations were compared against the equation in the commentary of CSA A23.3. The key findings of this study are outlined below.

- The newly defined parameters, $\psi_{rotation}$ and $\psi_{sliding}$, provide practical benefits by eliminating the need for nonlinear response history analysis to determine footing movement. These parameters can be calculated during the design process, offering engineers a more efficient way to estimate footing movements than previously available.
- The proposed equations for the footing rotation and sliding have a high coefficient of determination ($R^2 = 0.94$ for rotation and 0.87 for sliding), with normally distributed errors and homoskedasticity of residuals, indicating reliable and accurate predictions.
- Sensitivity analysis revealed that q_{unf}/q_{ult} is the most influential parameter for footing rotation, while T_f/T_{ult} is the most impactful for sliding. Both parameters measure the demand relative to the capacity.
- An artificial neural network (ANN) improved the accuracy of footing movement predictions by incorporating physical features with complex patterns or relationships resulting from combinations of predictor variables. The ANN models for rotation and sliding achieved higher R^2 values of 0.99 and 0.92, with an optimal number of neurons equal to 18 and 17, respectively.
- When sliding is insignificant, the proposed equations and the equation in the commentary of CSA A23.3 closely estimate footing rotation for CP footings. However, the CSA equation slightly underestimates rotation for smaller footings, such as not capacity-protected (NCP) footings.
- This study shows that the equation in the CSA A23.3 commentary fails to estimate footing movement accurately when sliding is significant. While Clause 21.10.3.3.3 of the CSA A23.3 standard seeks to address the issue of underestimated foundation motion by requiring at least 0.005 rad to be assumed for foundations that are smaller than CAN-CP, this can greatly overestimate the actual expected footing movement, leading to unnecessary conservatism in design.
- While the ANN-based models provide accurate predictions, they have certain shortcomings. Unlike Bayesian regression, which offers a transparent, explicit equation that highlights the most impactful predictor variables, ANN functions as a "black box." Although ANN achieves a somewhat higher prediction accuracy, the substantial uncertainty in input data, such as soil properties and earthquake demands, casts doubts on the practical value of this improvement. Therefore, the Bayesian regression model is recommended, even though ANN models can perform well in estimating footing movement.

The proposed equations can be integrated into foundation design requirements to optimize footing sizes and account for the effects of seismic loads and soil conditions. Although the equations are functions of general parameters that are not specific to the Canadian-designed buildings with concentrically braced frames (CBFs) that were used in this study, there is still a need for future research to verify that these equations also apply to buildings designed under other codes or with different types of lateral force-resisting systems. Furthermore, the Beam on Nonlinear Winkler Foundation (BNWF) model used here to simulate soil and foundation behavior does not account for the coupled effects of sliding and bearing strength, potentially influencing result accuracy.

CRediT authorship contribution statement

Hamid M. Madani: Writing – original draft, Validation, Methodology, Investigation, Formal analysis. **Lydell Wiebe:** Writing – review & editing, Supervision, Funding acquisition, Conceptualization. **Peijun Guo:** Writing – review & editing, Supervision, Funding acquisition. **Sanda Koboevic:** Writing – review & editing, Funding acquisition.

Declaration of Competing Interest

The authors of this manuscript have nothing to declare.

Acknowledgments

The authors acknowledge with gratitude the financial support of the Canadian Institute of Steel Construction (CISC) and the Natural Sciences and Engineering Research Council of Canada (NSERC). The authors also thank Andy Metten and Trevor Whitney (Bush, Bohlman & Partners LLP, Vancouver) for their contribution to design issues.

Data availability

Data will be made available on request.

References

[1] Miranda E, Aslani H. Probabilistic Response Assessment for Building-Specific Loss Estimation. PEER Rep. 2003/03. Pacific Earthquake Engineering Research Center. Berkeley, CA: University of California; 2003.
[2] Terzic V, Kolozvari K. Probabilistic evaluation of post-earthquake functional recovery for a tall RC core wall building using F-Rec framework. Eng Struct 2022; 253. https://doi.org/10.1016/j.engstruct.2021.113785.
[3] Molina Hutt C, Hulsey AM, Kakoty P, Deierlein GG, Eksir Monfared A, Wen-Yi Y, et al. Toward functional recovery performance in the seismic design of modern tall buildings. Earthq Spectra 2022;38:283–309. https://doi.org/10.1177/87552930211033620.
[4] Molina Hutt C, Vahanvaty T, Kourehpaz P. An analytical framework to assess earthquake-induced downtime and model recovery of buildings. Earthq Spectra 2022;38:1283–320. https://doi.org/10.1177/87552930211060856.

[5] FEMA (Federal Emergency Management Agency). Seismic Performance Assessment of Buildings, Methodology and Implementation. Rep. No. FEMA P-58-1. Washington, D.C.: 2018.

[6] Madani HM, Wiebe LDA, Guo P, Koboevic S. Effects of variability in soil properties on the seismic performance of CBF buildings. Can Conf - Pac Conf Earthq Eng, Vanc, BC, Can 2023.

[7] Madani H.M., Wiebe L.D.A., Koboevic S., Guo P. Seismic Force Demands on the Foundations of Concentrically Braced Frame Systems. 10th Int. Conf. Behav. Steel Struct. Seism. Areas, Timisoara, Romania: 2022..

[8] Madani H, Wiebe L, Guo P, Koboevic S. Towards more efficient footings for concentrically braced frames: effects of variability. 18th World Conf Earthq Eng, Milan, Italy 2024.

[9] Madani H.M., Wiebe L.D.A., Guo P., Koboevic S. Influence of Concentrically Braced Frame Footing Design on Recovery Time. Proc. 11th Int. Conf. Behav. Steel Struct. Seism. Areas, Salerno, Italy: 2024, p. 994–1005..

[10] Madani H.M., Wiebe L., Guo P., Koboevic S.. How soil-structure interaction and footing size affect seismic repair costs of low-rise concentrically braced frames. J Earthq Eng n.d.

[11] Allotey N, El Naggar MH. Analytical moment-rotation curves for rigid foundations based on a Winkler model. Soil Dyn Earthq Eng 2003;23:367–81. https://doi.org/10.1016/S0267-7261(03)00034-4.

[12] Pender MJ, Algie TB, Storie LB, Salimath R. Rocking Controlled Design of Shallow Foundations. Wellington, New Zealand: NZSEE Conf.; 2013.

[13] Bazargani P. Seism Demands Gravity-Load Columns Reinf Concr Shear wall Build [PhD Diss, Univ Br Columbia] 2014. https://doi.org/10.14288/1.0167436.

[14] Adebar P. Nonlinear rotation of capacity-protected foundations: The 2015 Canadian building code. Earthq Spectra 2015;31:1885–907. https://doi.org/10.1193/012814EQS022M.

[15] CSACanadian Standards Association). Design of concrete structures for buildings. CSA-A23.3:19. Mississauga, ON: 2019.

[16] Cement Association of Canada. Concrete Design Handbook. 4th ed. Ottawa, ON: 2017.

[17] NRCCNational Research Council of Canada). National Building Code of Canada. NBC-2020. Ottawa, ON: 2020.

[18] CSACanadian Standards Association). Design of steel structures for buildings. CSA-S16:19. Toronto, ON: 2019.

[19] American Society of Civil Engineers (ASCE). Minimum design loads and associated criteria for buildings and other structures. Reston, VA: 2022. doi:10.1061/9780784414248.

[20] McKenna F, Fenves GL, Scott MH, Jeremic B. Pacific Earthquake Engineering Research Center, University of California, Berkeley, CA. Open Syst Earthq Eng Simul (Open) 2000.

[21] Elkady A, Lignos DG. Effect of gravity framing on the overstrength and collapse capacity of steel frame buildings with perimeter special moment frames. Earthq Eng Struct Dyn 2015;44:1289–307. https://doi.org/10.1002/eqe.2519.

[22] Mohsenzadeh V, Wiebe L. Effect of beam-column connection fixity and gravity framing on the seismic collapse risk of special concentrically braced frames. Soil Dyn Earthq Eng 2018;115:685–97. https://doi.org/10.1016/j.soildyn.2018.09.035.

[23] Sen AD, Roeder CW, Lehman DE, Berman JW. Nonlinear modeling of concentrically braced frames. J Constr Steel Res 2019;157:103–20. https://doi.org/10.1016/j.jcsr.2019.02.007.

[24] Hsiao PC, Lehman DE, Roeder CW. Improved analytical model for special concentrically braced frames. J Constr Steel Res 2012;73:80–94. https://doi.org/10.1016/j.jcsr.2012.01.010.

[25] Lignos DG, Krawinkler H. Deterioration Modeling of Steel Components in Support of Collapse Prediction of Steel Moment Frames under Earthquake Loading. J Struct Eng 2011;137:1291–302. https://doi.org/10.1061/(ASCE)ST.1943-541X.0000376.

[26] NIST (National Institute of Standards and Technology). Guidelines for nonlinear structural analysis for design of buildings, part IIa – steel moment frames. Rep. No. NIST GCR 17-917-46v2. Gaithersburg, MD: 2017. doi:10.6028/NIST.GCR.17-917-46v2.

[27] Lignos DG, Hartloper AR, Elkady A, Deierlein GG, Hamburger R. Proposed Updates to the ASCE 41 Nonlinear Modeling Parameters for Wide-Flange Steel Columns in Support of Performance-Based Seismic Engineering. J Struct Eng 2019;145. https://doi.org/10.1061/(asce)st.1943-541x.0002353.

[28] Liu J, Astaneh-Asl A. Moment–Rotation Parameters for Composite Shear Tab Connections. J Struct Eng 2004:1371–80. https://doi.org/10.1061/(ASCE)0733-9445(2004)130.

[29] Harden C, Hutchinson T, Martin GR. Numerical Modeling of the Nonlinear Cyclic Response of Shallow Foundations. PEER Rep. 2005/04. Pacific Earthquake Engineering Research Center. Univ Calif, Berkeley, CA 2005.

[30] Gajan S, Hutchinson TC, Kutter BL, Raychowdhury P. Numerical Models for Analysis and Performance-Based Design of Shallow Foundations Subjected to Seismic Loading. PEER Rep. 2007/04. Pacific Earthquake Engineering Research Center, University of California. Berkeley, CA 2008.

[31] Wichman S, Berman JW, Lehman DE, Star L, Moresco J. Factors affecting the seismic collapse performance of realistic low-rise braced frame buildings, including soil structure interaction and foundation flexibility. Earthq Eng Struct Dyn 2022. https://doi.org/10.1002/eqe.3666.

[32] Gajan S, Raychowdhury P, Hutchinson TC, Kutter BL, Stewart JP. Application and validation of practical tools for nonlinear soil-foundation interaction analysis. Earthq Spectra 2010;26:111–29. https://doi.org/10.1193/1.3263242.

[33] FEMA (Federal Emergency Management Agency). A Practical Guide to Soil-Structure Interaction. Rep. No. FEMA P-2091. Washington, D.C.: 2020.

[34] NIST (National Institute of Standards and Technology). Soil-structure interaction for building structures. Rep. No. NIST GCR 12-917-21. Gaithersburg, MD: 2012.

[35] Canadian Geotechnical Society. Canadian Foundation Engineering Manual. 4th ed. Richmond, BC: 2006.

[36] Madani H.M. Towards more efficient shallow foundations for low-rise concentrically braced frame buildings. [PhD dissertation, McMaster University]. http://hdl.handle.net/11375/30900, 2024..

[37] Tremblay R, Atkinson GM, Bouaanani N, Daneshvar P, Léger P, Koboevic S. Selection and scaling of ground motion time histories for seismic analysis using NBCC. 11th Can Conf Earthq Eng 2015:2015. vol. 99060, Victoria, BC, Canada.

[38] Ancheta TD, Darragh RB, Stewart JP, Seyhan E, Silva WJ, Chiou BSJ, et al. NGA-West2 database. Earthq Spectra 2014;30:989–1005. https://doi.org/10.1193/070913EQS197M.

[39] National Research Institute for Earth Science and Disaster Resilience. NIED K-NET, KiK-net 2019. ⟨https://www.kyoshin.bosai.go.jp/⟩ (accessed June 26, 2023).

[40] CESMD. Center for Engineering Strong Motion Data Website. ⟨http://www.strongmotioncenter.org/⟩ (accessed June 26, 2023).

[41] Baker JW, Lee C. An Improved Algorithm for Selecting Ground Motions to Match a Conditional Spectrum. J Earthq Eng 2018;22:708–23. https://doi.org/10.1080/13632469.2016.1264334.

[42] Vamvatsikos D. Seismic Performance Uncertainty Estimation via IDA with Progressive Accelerogram-Wise Latin Hypercube Sampling. J Struct Eng 2014;140. https://doi.org/10.1061/(asce)st.1943-541x.0001030.

[43] Kazantzi AK, Vamvatsikos D, Lignos DG. Seismic performance of a steel moment-resisting frame subject to strength and ductility uncertainty. Eng Struct 2014;78:69–77. https://doi.org/10.1016/j.engstruct.2014.06.044.

[44] Madani H.M., Wiebe L., Guo P., Koboevic S.. Functional recovery of low-rise concentrically braced frame buildings: probabilistic assessment of footing size effects. Earthq Spectra n.d.

[45] Mahsuli M. PhD dissertation, University of British Columbia. Probabilistic Models, Methods, Softw Eval risk Civ Infrastruct 2012. https://doi.org/10.14288/1.0050878.

[46] Mahsuli M, Haukaas T. Computer Program for Multimodel Reliability and Optimization Analysis. J Comput Civ Eng 2013;27:87–98. https://doi.org/10.1061/(ASCE)CP.1943-5487.0000204.

[47] Gardoni P, Der Kiureghian A, Mosalam KM. Probabilistic capacity models and fragility estimates for reinforced concrete columns based on experimental observations. J Eng Mech 2002;128:1024–38. https://doi.org/10.1061/(ASCE)0733-9399(2002)128:10(1024).

[48] Tu JV. Advantages and disadvantages of using artificial neural networks versus logistic regression for predicting medical outcomes. J Clin Epidemiol 1996;49:1225–31.

[49] Schmidt M, Lipson H. Distilling free-form natural laws from experimental data. Science (80-) 2009;324:81–5. https://doi.org/10.1126/science.1165893.

[50] Negro P., Verzeletti G., Molina J., Pedretti S., Lo Presti D., Pedroni S. Large-scale geotechnical experiments on soil–foundation interaction. Special Publication No. I.98.73, Joint Research Center, European Commission, Ispra, Italy: 1998..